Molybdenum isotope and trace metal signals in an iron-rich Mesoproterozoic ocean: A snapshot from the Vindhyan Basin, India

Geoffrey J. Gilleaudeau[a,*,1], Swapan K. Sahoo[b,c,*,1], Chadlin M. Ostrander[d], Jeremy D. Owens[e], Simon W. Poulton[f], Timothy W. Lyons[g], Ariel D. Anbar[d,h]

[a] Department of Atmospheric, Oceanic, and Earth Sciences, George Mason University, Fairfax, VA, USA
[b] Department of Geoscience, University of Nevada, Las Vegas, NV, USA
[c] Equinor US, Houston, TX, USA
[d] School of Earth and Space Exploration, Arizona State University, Tempe, AZ, USA
[e] Department of Earth, Ocean, and Atmospheric Science, National High Magnetic Field Laboratory, Florida State University, Tallahassee, FL, USA
[f] School of Earth and Environment, University of Leeds, Leeds, UK
[g] Department of Earth and Planetary Sciences, University of California, Riverside, CA, USA
[h] School of Molecular Sciences, Arizona State University, Tempe, AZ, USA

ARTICLE INFO

ABSTRACT

Fundamental questions persist regarding the redox structure and trace metal content of the Mesoproterozoic oceans. Multiple lines of evidence suggest more widespread anoxia in the deep oceans compared to today, and iron speciation indicates that anoxia was largely accompanied by dissolved ferrous iron (ferruginous conditions) rather than free sulfide (euxinia). Still, exceptions exist—euxinic conditions have been reported from some ocean margin and epeiric sea settings, and oxic conditions were reported in one deeper water environment and are also known from shallow waters. Constraining the temporal evolution of Mesoproterozoic marine redox structure is critical because it likely governed redox-sensitive trace metal availability, which in turn played a significant role in marine diazotrophy and the evolution of early eukaryotes. Here, we present a new, multi-proxy geochemical dataset from the ~1.2 Ga Bijaygarh Shale (Kaimur Group, Vindhyan Basin, India) emphasizing total organic carbon, iron speciation, and trace metal concentrations, as well as sulfur, nitrogen, and molybdenum isotopes. This unit was deposited in an open shelf setting near or just below storm wave base. Taken together, our data provide a unique snapshot of a biologically important shallow shelf setting during the Mesoproterozoic Era, which includes: 1) locally ferruginous waters below the zone of wave mixing, 2) muted enrichment of trace metals sensitive to general anoxia (e.g., chromium) and variable enrichment of trace metals sensitive to euxinia (e.g., molybdenum and, to a lesser extent, vanadium), 3) general sulfate limitation, and 4) nitrogen fixation by molybdenum-nitrogenase and a dominantly anaerobic nitrogen cycle in offshore settings. Differential patterns of trace metal enrichment are consistent with data from other basins and suggest a largely anoxic ocean with limited euxinia during the Mesoproterozoic Era. Our new molybdenum isotope data—the first such data from unambiguously marine shales deposited between 1.4 and 0.75 Ga—record values up to $+1.18 \pm 0.12‰$ that are analogous to data from other Mesoproterozoic shale units. Ultimately, this study provides a broad, multi-proxy perspective on the redox conditions that accompanied early eukaryotic evolution.

1. Introduction

The Mesoproterozoic Era (1.6 to 1.0 billion years ago; Ga) is a critical interval in Earth evolution characterized by increasing diversity of early eukaryotes in shallow marine settings (Javaux et al., 2001; Beghin et al., 2017). These changes occurred against a backdrop of low but potentially variable atmospheric O_2 concentrations (Planavsky et al., 2014; Cole et al., 2016; Gilleaudeau et al., 2016), although there is a lack of agreement about how low. Despite potential linkages between oxygen and evolution, the redox state of the Mesoproterozoic atmosphere and oceans remains poorly constrained. Previous iron speciation studies have reported mostly locally anoxic and iron-rich (ferruginous)

* Corresponding authors at: Department of Atmospheric, Oceanic, and Earth Sciences, George Mason University, Fairfax, VA, USA (G.J. Gilleaudeau), Department of Geoscience, University of Nevada, Las Vegas, NV, USA (S.K. Sahoo).
E-mail addresses: ggilleau@gmu.edu (G.J. Gilleaudeau), swas@equinor.com (S.K. Sahoo).
[1] These authors contributed equally to this work.

conditions in subsurface waters (Planavsky et al., 2011; Sperling et al., 2015; Doyle et al., 2018; Zhang et al., 2018)—however, both oxic and sulfidic conditions have also been reported in epeiric sea, open shelf, and basinal settings (e.g., Shen et al., 2002; 2003; Gilleaudeau and Kah, 2013; 2015; Sperling et al., 2014; Cox et al., 2016). Predominantly low marine oxygen levels are also evidenced by muted enrichment of redox-sensitive trace metals in many Mesoproterozoic-aged shales (e.g., Scott et al., 2008), as well as by both molybdenum (Arnold et al., 2004; Kendall et al., 2011) and, potentially, uranium isotope (Gilleaudeau et al., 2019) data. Despite evidence for largely anoxic Mesoproterozoic oceans, several transient oxygenation episodes have recently been proposed based on a variety of geochemical evidence, most notably at ~1.56 Ga (Zhang et al., 2018), 1.4 Ga, and 1.1 Ga (Diamond and Lyons, 2018). Little is known, however, about the redox state of the global oceans in the interval between these purported oxygenation events, and, more generally, temporal gaps in the Mesoproterozoic record challenge our understanding of co-evolving life and environments during this interval.

Here, we present a comprehensive, multi-proxy dataset from the ~1.2 Ga Bijaygarh Shale, Vindhyan Basin, India. We use total organic carbon (TOC), iron speciation, and trace metal abundances, as well as sulfur (S), nitrogen (N), and Mo isotope data to provide robust new constraints on both local and global redox cycling in the Mesoproterozoic ocean. This study provides the first Mo isotope data from unambiguously marine shale of late Mesoproterozoic age (see also Stüeken et al., 2017) and should inform future reconstructions of the environmental conditions that accompanied early eukaryotic diversification and the broader linkages between ocean oxygenation and biospheric evolution.

2. Geologic background

2.1. Regional geology

The Vindhyan Supergroup is one of the largest and thickest Proterozoic sedimentary sequences in the world, with an areal extent of ~100,000 km^2 (Gopalan et al., 2013). It is best described as an intracratonic basin and is composed mostly of shallow marine deposits, with a significant part of the basin currently covered under Gangetic alluvium in the north and the Deccan traps in the southwest (Chakraborty, 2006; Ray, 2006). The basin was first developed by rifting on the Aravalli craton along an E-W oriented fault system (Bose et al., 2001). Sedimentary units overlie the ~2.5 Ga (Azmi, 1998) Bundelkhand igneous complex and metamorphosed Paleoproterozoic rocks of the Bijawar and Gwalior groups (Mazumder et al., 2000). The basin is bounded by arcuate fault lineaments comprising the Great Boundary Fault to the northwest and by the Narmada-Son lineament to the southeast—restrained by the Aravalli-Delhi fold belt (ADFB) and the Central India Tectonic Zone (CITZ), respectively.

Vindhyan Basin sedimentary strata are up to 4500 m thick and are exposed in two main outcrop belts—in Son Valley (Madhya and Uttar Pradesh) and in Rajasthan (Fig. 1). These two terranes are separated by a basement ridge that exposes trondhjemitic gneisses of the Bundelkhand complex (Prasad and Rao, 2006). The sedimentary sequences are subdivided into the Lower Vindhyan sequence (the Semri Group) and the Upper Vindhyan sequence (the Kaimur, Rewa, and Bhander groups) separated by a major hiatus of unknown duration (Bose et al., 2001; Ray, 2006) (Fig. 2). The litho-units of the Semri Group are dominated by carbonate and shale, along with sandstone and volcaniclastic deposits (Ramakrishnan and Vaidyanadhan, 2008). Above the unconformity, the Kaimur and Rewa groups are almost entirely siliciclastic in both Son Valley and Rajasthan. The Kaimur Group, the oldest unit of the Upper Vindhyan sequence, is primarily composed of sandstone, shale, and conglomerate, including the Bijaygarh Shale—the focus of this study (Fig. 2). In Son Valley, the Kaimur Group lies unconformably on the Semri Group, and this contact is often characterized

by a conglomeratic layer that sits directly above the unconformity. The Rewa Group is dominated by shale and sandstone with interbedded carbonate. The lower part of the Rewa Group is not well exposed in the southern Son Valley; however, the overlying units are correlatable across the basin (Chakraborty, 2006). The presence of red shale, limestone, and glauconitic siltstone is indicative of shallow shelf deposition. By contrast, the Bhander Group contains a prominent carbonate unit: the Bhander Limestone in Son Valley and the Lakheri Limestone in Rajasthan, both of which are bounded above and below by thick successions of clastic rocks. The Bhander Group is characterized by a sandstone-shale-stromatolitic limestone sequence, with deposition occurring mainly in tidal flat and shelf environments (Bose et al., 2001; Ramakrishnan and Vaidyanadhan, 2008).

Overall, paleocurrent analysis (Bose et al., 2001) and the basin-scale presence of tidal current and wave features (Banerjee, 1982; Chakraborty and Bose, 1990) suggest that Vindhyan Basin units were deposited in an epicratonic sea with open ocean connection to the northwest (Chanda and Bhattacharya, 1982). Vindhyan Basin strata are largely unmetamorphosed and are only mildly deformed.

2.2. Age constraints

The age of the Lower Vindhyan sequence is well constrained by a series of geochronological studies in the Semri Group. Magmatic zircons extracted from ash beds in the Porcellanite Formation yielded U-Pb ages of 1628 ± 8 Ma (Rasmussen et al., 2002) and 1630.7 ± 0.8 Ma (Ray et al., 2002). A similar age of 1640 ± 4 Ma was determined using U-Pb geochronology on magmatic zircons from rhyolite flows in the Porcellanite Formation (Bickford et al., 2017). Higher in the Semri Group succession, an ash bed in the Rampur Shale yielded a U-Pb zircon age of 1599 ± 8 Ma (Rasmussen et al., 2002). These represent the most precise age dates published thus far on the Lower Vindhyan sequence and constrain its deposition tightly between ~1700 and 1600 Ma.

In contrast, the age of the Upper Vindhyan sequence has been the subject of controversy. The onset of sedimentation in the Upper Vindhyan sequence is constrained as older than 1073.5 ± 13.7 Ma based on a phlogopite Ar-Ar age in the Majhgawan kimberlite, which intrudes lowermost Kaimur Group strata (Gregory et al., 2006). Initially, the overlying units of the Rewa and Bhander groups were thought to be late Neoproterozoic in age based on Sr-isotope stratigraphy (Ray et al., 2003) and reports of enigmatic Ediacara-type fossils (De, 2006). In recent years, however, abundant evidence has suggested a substantial revision to an older, Mesoproterozoic age for the Upper Vindhyan sequence. This evidence includes paleomagnetic comparison to the Majhgawan kimberlite (Malone et al., 2008), a compilation of detrital zircon ages (McKenzie et al., 2011; 2013; Turner et al., 2014), Pb-Pb geochronology on Bhander Group carbonate units (Gopalan et al., 2013), and carbon isotope stratigraphy in the Bhander Group (Gilleaudeau et al., 2018). Lastly—and most importantly for this study—Tripathy and Singh (2015) presented a Re-Os age of 1210 ± 52 Ma for the Bijaygarh Shale, which we use as the basis for the remainder of our discussion.

2.3. Depositional setting of the Bijaygarh Shale

The Bijaygarh Shale lies gradationally above the Lower Kaimur Sandstone and is thought to represent maximum transgression in the Vindhyan Basin (Banerjee et al., 2006). In proximal settings near the Amjhore Pyrite Mines (Bihar Province), the Bijaygarh Shale is an organic-rich unit that is characterized by interlayered siltstone and hummocky cross-stratified sandstone, with abundant gutter casts at the base of the decimeter-thick sandstone beds (Chakraborty, 1995). These features are indicative of periodic storm incursions and suggest deposition in an inner shelf setting above storm wave base (Banerjee et al., 2006). Our samples were collected near Churk village further to the west (Uttar Pradesh). Here, homogenous, non-fissile black shale is
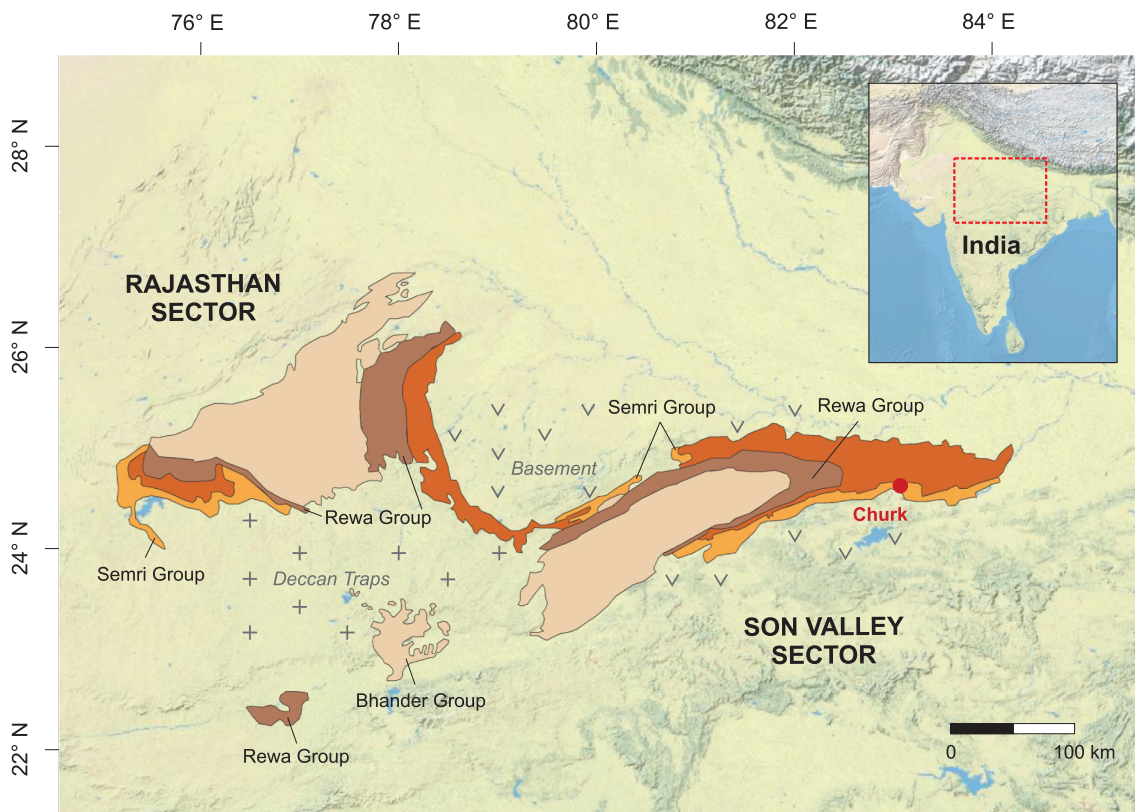
Fig. 1. Generalized geologic map of the Vindhyan Basin in north-central India. Geology based on Ray et al. (2003) and figure from Gilleaudeau et al. (2018) with base map generated in ArcGIS using the U.S. National Park Service Natural Earth physical map.

exposed, and there are limited sandy or silty intervals that could indicate periodic storm activity. This relationship is consistent with deposition of our samples in a more distal shelf setting near or below storm wave base.

3. Methods

3.1. Sample collection and preparation

Bijaygarh Shale samples were collected from a railroad outcrop section near the township of Churk, Uttar Pradesh (24° 37′ 04.9″ N, 83° 06′ 19.2″ E) (Fig. 2). For the present work, fresh samples were collected at an average spacing of 1–2 m. Any macroscopic pyrites and fractured/weathered samples were avoided. Subsequently, samples were

powdered under metal-free conditions. The Churk section was chosen to explore more distal environments of the Bijaygarh Shale, compared to the more proximal Amjhore mine sections previously studied by Sarkar et al. (2010), Tripathy and Singh (2015), and Singh et al. (2018).

3.2. Total organic carbon (TOC)

Total organic carbon (TOC) contents were determined by difference between carbonate-carbon liberated by 4 M HCl and total carbon released by combustion at 1400 °C, both of which were measured with an ELTRA C/S analyzer in the Biogeochemistry Laboratory at the University of California, Riverside (UCR). Analytical precision for TOC monitored by duplicates is better than 0.1%.
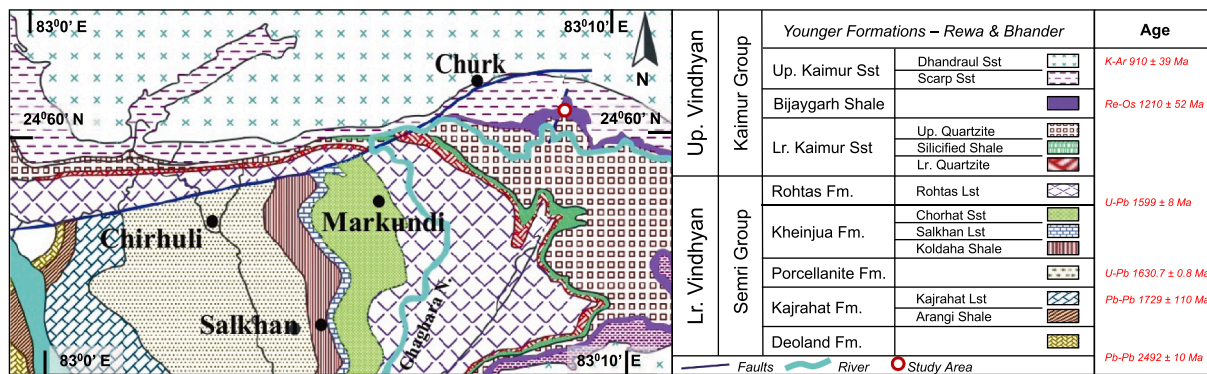

Fig. 2. Regional geologic map (left) with study location highlighted by red circle. Generalized Vindhyan Basin stratigraphy (right) with relevant radiometric age constraints. Geochronology from Rasmussen et al. (2002), Ray et al. (2002), and Tripathy and Singh (2015), and figure modified from Quasim and Ahmad (2015). (For interpretation of the references to colour in this figure legend, the reader is referred to the web version of this article.)

Table 1
Molybdenum isotope data from standard reference material solutions.

Standard	$\delta^{98}Mo$[a]	n	Normalized to NIST + 0.25‰[b]	Goldberg et al. (2013)
ICL-Mo	+0.14 ± 0.04‰	4	+0.06 ± 0.04‰	+0.09 ± 0.05‰
Kyoto-Mo	−0.05 ± 0.04‰	4	−0.13 ± 0.04‰	−0.12 ± 0.06‰
NIST SRM 3134	+0.33 ± 0.06‰	7	+0.25	+0.25
SDO-1[c]	+1.11 ± 0.03‰	7	+1.03 ± 0.03‰	+1.05 ± 0.14‰

*All reported errors are 2SD of the standard reproducibility.
  [a] Measured relative to Roch-Mo2.
  [b] The new international reporting standard (Nagler et al., 2014).
  [c] This SDO-1 was a separate standard solution, and not the SDO-1 that was processed alongside our samples.

3.3. Iron speciation and trace metal abundances

Iron speciation analyses were conducted at UCR following published methods (Poulton and Canfield, 2005). Pyrite iron (Fe_{py}) was calculated (assuming a stoichiometry of FeS_2) from the weight percentage of sulfur extracted during a two-hour hot chromous chloride distillation followed by iodometric titration (Canfield et al., 1986). Other iron species—-specifically, Fe_{carb}, Fe_{ox}, and Fe_{mag}—were extracted sequentially (Poulton and Canfield, 2005) using sodium acetate solution, dithionite solution, and ammonium oxalate solution, respectively. The sequential extracts were analyzed with an Agilent 7500ce inductively-coupled plasma mass spectrometer (ICP-MS). As mentioned below, total iron concentrations (Fe_T) were determined by HF-HNO_3-HCl acid digestion followed by ICP-MS analysis. Reproducibility of iron measurements, monitored by duplicate analyses, was better than 6% relative percent deviation (2SD).

Major and trace elemental abundances were analyzed at the W. M. Keck Foundation Laboratory for Environmental Biogeochemistry at Arizona State University (ASU) and at UCR following previously published methods (Poulton et al., 2004; Scott et al., 2008, Kendall et al., 2010). Samples were ashed for 8–10 h at 550 °C and dissolved completely during an acid digestion with HF-HNO_3-HCl. Trace and major element concentrations were determined on a ThermoFinnigan X-Series (ASU) or Agilent 7500ce (UCR) quadrupole ICP-MS. Accuracy and precision were monitored with duplicate samples and by analysis of the USGS Devonian black shale standard (SDO-1). Reproducibility in individual runs was better than 5% relative percent deviation (2SD) for the presented elements.

3.4. Sulfur isotopes

Pyrite sulfur was extracted for isotope measurements using chromous chloride distillation and re-precipitation of pyrite sulfur as Ag_2S. Sulfur isotope measurements ($\delta^{34}S$) were made with a ThermoFinnigan Delta V continuous-flow stable-isotope-ratio mass spectrometer at UCR. Sulfur isotope data are reported as per mil (‰) deviations from the isotopic composition of the Vienna Cañon Diablo Troilite (VCDT). Reproducibility was better than 0.2‰ on the basis of single-run and long-term standard monitoring.

3.5. Nitrogen isotopes

Nitrogen isotope compositions ($\delta^{15}N$) of decarbonated whole-rock samples were analyzed at the LVIS lab in the Department of Geoscience, University of Nevada, Las Vegas, following previously published procedures (e.g., Maharjan et al., 2018). Sample powders were decarbonated using acid fumigation with 6 N HCl. The carbonate-free residue was then rinsed with deionized water repeatedly until a neutral pH was reached. After drying in an oven at 70 °C for 4 h, isotopic values were measured using an elemental analyzer (EA) coupled with a Conflow interface that automatically transfers gas generated by sample combustion into a Finnigan Delta Plus mass spectrometer. Nitrogen isotope values are reported as standard per mil (‰) deviations from atmospheric N_2. Uncertainties determined by duplicates of acetanilide are better than 0.3‰ for $\delta^{15}N$.

3.6. Molybdenum isotopes

All Mo isotope analyses, and their associated preparation, took place at the W.M. Keck Foundation Laboratory for Environmental Biogeochemistry, School of Earth and Space Exploration, Arizona State University. First, appropriate amount of sample aliquot was removed from each total digestion solution to provide 125 ng of Mo. These samples were then spiked with an optimal amount of calibrated synthetic Mo-isotope double-spike (^{97}Mo and ^{100}Mo) before purification via ion exchange chromatography (Barling et al., 2001). The double spike is used for chromatography and instrumental mass fractionation correction.

Isotope ratio measurements were performed on a Thermo Neptune multi-collector inductively coupled plasma mass spectrometer (MC-ICP-MS) in low-resolution mode with an Elemental Scientific Inc. Apex inlet system. All measurements were made using the Johnson Matthey Specpure Mo plasma standard (Lot no. 802309E; Roch-Mo2) as the bracketing standard and then re-calculated relative to the international NIST SRM 3134 standard with a $\delta^{98}Mo$ value of +0.25‰ (Nagler et al., 2014). These calculations were informed by measurement of the NIST SRM 3134 standard relative to Roch-Mo2 during our analytical sessions (Table 1). Samples and standards were analyzed at a concentration of 15 ng/g^{-1} Mo, which yielded about 0.6 V of signal on mass 98. Each sample was measured in duplicate, with an average 2SD sample reproducibility of 0.10‰ and a maximum of 0.12‰. USGS rock reference material SDO-1 (Devonian Ohio Shale) was simultaneously processed with our set of samples to monitor accuracy and showed good reproducibility with a previous study (Goldberg et al., 2013; $\delta^{98}Mo$ = +0.95 ± 0.05‰ [2SD] compared with +1.05 ± 0.14‰) and with various secondary standard solutions (Table 1). Finally, for each analytical run, we measured a series of standards with varying spike/sample ratios. All samples were within the validated spike/sample range for accurate and precise $\delta^{98}Mo$ values.

4. Results

We first visually inspected rock samples collected from the railroad section in order to assess the potential for oxidative diagenesis to impact iron speciation and trace metal signals. Finely disseminated pyrite was observed under magnification with no evidence for oxidized rims or leaching of iron into the surrounding shale. This gives us confidence that oxidative remobilization has not affected our geochemical signals. Samples from the Bijaygarh Shale are relatively organic-rich, with TOC values ranging from 0.92 to 5.87 wt%. There is a general increase in TOC values up section, with the exception of the uppermost sample, which records the lowest value. Ratios of highly reactive iron to total iron (Fe_{HR}/Fe_T)—a proxy for anoxia (see Section 5.1)—are low in the lower three meters of the section (0.10 to 0.16) but increase markedly thereafter and remain high for the rest of the section (0.48 to 1.00). By contrast, ratios of pyrite iron to highly reactive iron (Fe_{py}/Fe_{HR})—a proxy for distinguishing ferruginous from euxinic anoxic conditions (see Section 5.1)—are high in the lower four meters of the section (0.64–1.00) but decrease markedly thereafter and remain low for the rest of the section (0.08–0.32 with the exception of one sample).

Concentrations of redox-sensitive elements are reported as enrichment factors (EF) relative to bulk upper continental crust (UCC). Enrichment factors were calculated relative to aluminum (Al) by the standard approach (EF of element X = $(X/Al)_{sample}/(X/Al)_{UCC}$ using UCC element abundances reported by Rudnick and Gao (2003)). In our samples, molybdenum (Mo) concentrations range from 2 to 34 ppm,

Table 2
Total organic carbon, isotope, and elemental data for the Bijaygarh Shale.

Sample	Height (m)	TOC (wt. %)	$\delta^{34}S_{PY}$ (‰)	$\delta^{15}N$ (‰)	$\delta^{98}Mo$ (‰)*	Al (wt. %)	Fe (wt. %)	Mo (ppm)	V (ppm)	Cr (ppm)	U (ppm)	Mo EF^	V EF^	Cr EF^	U EF^
BS-C-1	1	1.82		+1.9	+1.09	8.11	1.04	2.0	109.0	55.2	5.3	1.8	1.1	0.6	2.0
BS-C-2	2	1.80		+0.6	+1.01	6.88	0.84	1.7	82.9	47.8	5.4	1.9	1.0	0.6	2.4
BS-C-3	3	2.02		+1.9	+0.89	7.46	1.04	3.2	99.2	54.9	12.0	3.2	1.1	0.7	4.8
BS-C-4	4	2.18		+1.3	+0.54	1.80	0.25	4.1	70.4	13.2	14.1	16.9	3.3	0.7	23.7
BS-C-5	5	2.23		+2.3	+1.11	1.57	0.88	11.6	43.1	14.7	25.7	54.8	2.3	0.8	49.4
BS-C-6	6	4.48	+14.8	+1.8	+1.18	3.41	2.10	33.3	281.4	30.6	17.2	72.3	6.9	0.8	15.2
BS-C-7	7	2.96		+2.8	+0.71	1.69	1.12	13.4	78.6	15.4	13.2	58.8	3.9	0.8	23.5
BS-C-8	8	1.41		+1.2	+0.80	2.00	0.75	6.3	76.0	14.0	11.0	23.4	3.2	0.6	16.5
BS-C-9	9	5.87	+21.5	+2.9	+1.10	3.87	2.69	29.4	320.9	32.6	22.0	56.3	7.0	0.7	17.2
BS-C-10	10	3.07	+20.7	+2.7	+1.18	3.33	1.88	22.2	159.8	26.8	23.7	49.5	4.0	0.7	21.5
BS-C-11	11	4.34	+21.2	+1.5	+0.93	3.59	2.49	12.7	186.9	34.2	13.3	26.3	4.4	0.8	11.2
BS-C-12	12	5.67	+25.0	+1.8	+0.96	3.94	2.06	23.9	295.4	33.8	21.2	45.0	6.3	0.8	16.2
BS-C-14	14	4.99	+18.5	+2.0	+1.15	3.04	3.10	17.8	163.7	26.6	14.3	43.3	4.5	0.8	14.2
BS-C-15	15	6.07	+21.1	+1.5	+1.10	3.83	3.19	33.5	306.1	29.1	24.4	64.9	6.7	0.7	19.3
BS-C-18	18	0.92		+0.3	−0.27	3.21	2.72	2.0	30.0	17.7	2.9	4.7	0.8	0.5	2.7

*Molybdenum isotopes are reported as $\delta^{98}Mo$ (NIST SRM 3134 standard + 0.25‰ (Nagler et al., 2014)). 2SD on all $\delta^{98}Mo$ values is 0.10‰, except for sample BS-C-6 where the 2SD is 0.12.
^Element enrichment factors (EF) calculated using: EF of element X = $(X/Al)_{sample}/(X/Al)_{UCC}$, where UCC refers to the upper continental crust value of Rudnick and Gao (2003). UCC values were set to 1.1, 97, 92, and 2.7 ppm for Mo, V, Cr, and U, respectively, along with 8.15 wt% for Al (Rudnick and Gao, 2003).

and Mo EF ranges from 1.8 to 64.9. In the lower three meters, Mo EF does not exceed 3.2. There is a sharp increase above three meters, however, in both [Mo] and Mo EF such that Mo EF remains above 16.9 for the remainder of the section (except for the uppermost sample). Vanadium (V) concentrations range from 30 to 306 ppm in our samples, and V EF ranges from 0.8 to 7.0. Similar to Mo, V EF does not exceed 1.1 in the lower three meters but increases to values greater than 2.3 for the remainder of the section (except for the uppermost sample). Chromium (Cr) concentrations range from 13 to 55 ppm, and Cr EF is persistently low, never exceeding 0.8 at any point in the section (see Section 5.2. for discussion). Uranium (U) concentrations range from 3 to 26 ppm and are enriched substantially above crustal values (U EF between 2.0 and 49.4). As for the other elements, U EF remains low (below 4.8) in the lower three meters but increases sharply to values not less than 11.2 for the remainder of the section (except for the uppermost sample).

$\delta^{34}S$ values for pyrite are positive and range from +14.8 to +25.0‰, and $\delta^{15}N$ values for decarbonated whole-rock samples are slightly positive, ranging from +0.3 to +2.9‰. Neither isotope system exhibits systematic stratigraphic trends. Lastly, $\delta^{98}Mo$ values in our dataset range from −0.27 ± 0.06‰ to +1.18 ± 0.12‰ with no systematic stratigraphic trend. Raw data are presented in Tables 2 and 3, and stratigraphic plots for each of these parameters are presented in Fig. 3. An iron speciation cross-plot is presented in Fig. 4, and trace metal EF cross-plots are presented in Figs. 4 and 5.

5. Discussion

5.1. Local redox conditions

The relative distribution of iron among biogeochemically reactive phases in sediments is highly dependent on local redox conditions, such that iron speciation can serve as a powerful proxy for past ocean oxygenation. Highly reactive iron (Fe_{HR}) is defined as the sum of iron phases that are reactive to sulfide during early diagenesis (commonly iron carbonate, iron (oxyhydr)oxides, or magnetite), as well as pyrite (Fe_{py})—the product of that reaction (Raiswell and Canfield, 1998). Sediments become enriched in Fe_{HR} relative to total iron (Fe_T) under anoxic conditions through the addition of reactive iron minerals from the water column (Canfield et al., 1996; Lyons and Severmann, 2006). Under anoxic conditions, Fe_{HR}/Fe_T will typically exceed 0.38 (Raiswell and Canfield, 1998). By contrast, Fe_{HR}/Fe_T ratios of less than 0.22 are considered to represent oxic depositional conditions, and Fe_{HR}/Fe_T between 0.22 and 0.38 is ambiguous (Poulton and Canfield, 2011).

Identifying which reactive iron minerals are present in Fe_{HR}-enriched samples is key for determining if anoxia was accompanied by dissolved iron (ferruginous conditions) or sulfide (euxinic conditions). Under ferruginous conditions, iron carbonate, iron (oxyhydr)oxides, and magnetite typically dominant the Fe_{HR} pool, whereas under euxinic conditions, the Fe_{HR} pool is dominated by pyrite. Empirical data from modern anoxic basins suggest that a Fe_{py}/Fe_{HR} ratio that exceeds 0.8 is a reliable fingerprint for euxinic conditions, whereas Fe_{py}/Fe_{HR} less than 0.8 is indicative of ferruginous conditions (Anderson and Raiswell, 2004). Some studies, however, place this Fe_{py}/Fe_{HR} cutoff value at 0.7 (e.g., März et al., 2008). Ideally, the data fall well above or below these threshold values, minimizing any ambiguities.

In the Bijaygarh Shale, the lower three meters are characterized an Fe_{HR}/Fe_T signal suggestive of oxic conditions but with elevated Fe_{py}/Fe_{HR} ratios. This pairing is often interpreted as indicative of an oxic water column above sulfide-rich pore waters (Gilleaudeau and Kah, 2015; Sperling et al., 2015; Hardisty et al., 2018), but could also indicate high sedimentation rates that are masking an anoxic signal. Indeed, the lower part of the section contains three visible decimeter-

Table 3
Iron speciation data for the Bijaygarh Shale.

Sample	Height (m)	Fe_{PY} (wt. %)	Fe_{OX} (wt. %)	Fe_{MAG} (wt.%)	Fe_{CARB} (wt.%)	Fe_{HR}/Fe_T	Fe_{PY}/Fe_{HR}
BS-C-1	1	0.11	0.00	0.00	0.00	0.10	1.00
BS-C-2	2	0.13	0.00	0.01	0.00	0.16	0.95
BS-C-3	3	0.11	0.05	0.01	0.00	0.16	0.64
BS-C-4	4	0.11	0.02	0.01	0.00	0.51	0.82
BS-C-5	5	0.10	0.73	0.02	0.00	1.00	0.12
BS-C-6	6	1.81	0.51	0.11	0.00	1.00	0.74
BS-C-7	7	0.12	1.57	0.17	0.00	1.00	0.06
BS-C-8	8	0.10	0.47	0.02	0.00	0.78	0.16
BS-C-9	9	0.20	1.69	0.35	0.00	0.83	0.09
BS-C-10	10	0.64	1.39	0.00	0.00	1.00	0.32
BS-C-11	11	0.42	1.96	0.04	0.00	1.00	0.17
BS-C-12	12	0.40	1.55	0.03	0.00	1.00	0.20
BS-C-14	14	0.40	2.91	0.04	0.00	1.00	0.12
BS-C-15	15	0.37	1.60	0.70	0.00	0.84	0.14
BS-C-18	18	0.10	0.90	0.32	0.00	0.48	0.08

*Fe_{py} was determined by a chromium-reducible sulfide extraction, Fe_{ox} was determined using a dithionite extraction, Fe_{mag} was determined using an oxalate extraction, and Fe_{carb} was determined using an acetate extraction.
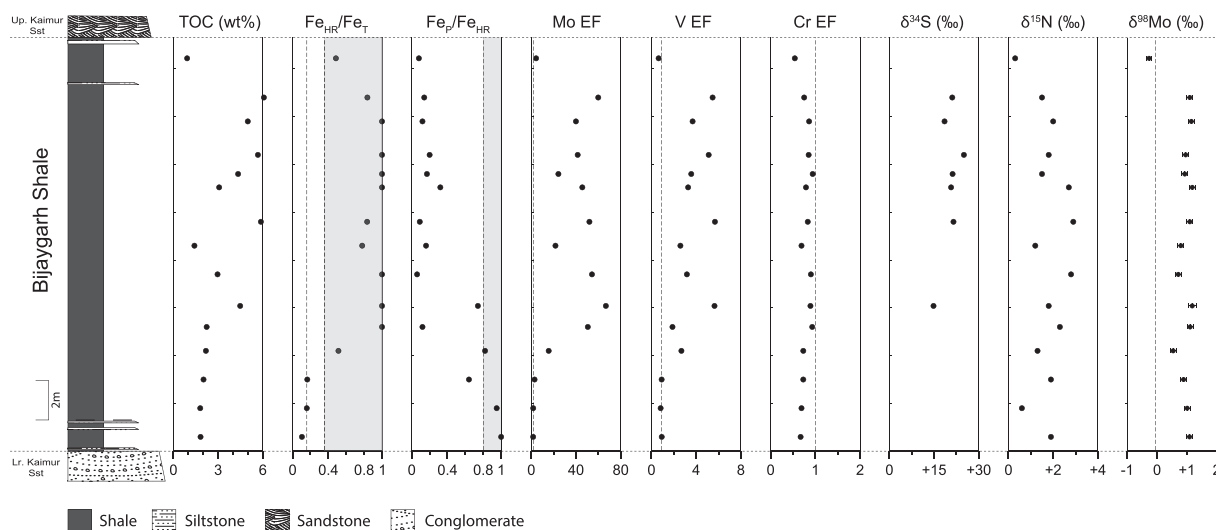
Fig. 3. Stratigraphic plot of iron speciation, trace metal, and isotopic data for the ~1.2 Ga Bijaygarh Shale. For nitrogen and sulfur isotopes, 2SD analytical uncertainties are smaller than the data point. For molybdenum isotopes, 2SD analytical uncertainties are included with each data point. In the iron speciation plots, shaded grey areas represent anoxic values for Fe_{HR}/Fe_T and euxinic values for Fe_{py}/Fe_{HR}.

scale siltstone beds that could indicate higher sedimentation rates in slightly more proximal environments. In the remainder of the section, iron speciation suggests deposition under ferruginous conditions. Since the Bijaygarh Shale was deposited during maximum transgression in an open shelf setting near storm wave base (Banerjee et al., 2006), our iron speciation data suggest that anoxic, ferruginous conditions developed directly below the zone of wave mixing during relative sea-level high-stand in the Vindhyan Basin.

Combined with data from other basins, iron speciation indicates a high degree of redox spatiotemporal heterogeneity in the Mesoproterozoic oceans. Euxinic conditions have been documented in nearshore settings in the ~1.7 to 1.4 Ga McArthur and Roper basins of Australia (Shen et al., 2002; 2003; Cox et al., 2016; Nguyen et al., 2019) and the ~1.1 Ga Taoudeni Basin of Mauritania (Gilleaudeau and Kah, 2013; 2015). Evidence for Mesoproterozoic euxinia also comes from organic biomarkers (Brocks et al., 2005; Blumenberg et al., 2012) and mass-independent mercury isotope data (Zheng et al., 2018). By contrast, Sperling et al. (2014) presented iron speciation evidence for oxic conditions at depth in the ~1.4 Ga Kaltasy Formation, Russia. However, a compilation of iron speciation data from deeper Mesoproterozoic settings revealed dominantly ferruginous conditions (Planavsky et al.,

2011)—a conclusion that has been confirmed by subsequent iron speciation studies (Sperling et al., 2015; Beghin et al., 2017; Doyle et al., 2018; Zhang et al., 2018). It seems, then, that the Mesoproterozoic oceans may have been weakly redox-buffered with frequent fluctuation in space and time between euxinic and ferruginous conditions (Planavsky et al., 2018), with evidence for at least weakly and intermittently oxic conditions in surface waters (e.g., Hardisty et al., 2017).

Recent quantitative constraints on Mesoproterozoic ocean redox come from statistical analysis of iron speciation data (Sperling et al., 2015), differential trace metal enrichment patterns in marine shale (Reinhard et al., 2013; Sheen et al., 2018), and uranium isotope analysis of marine carbonate (Gilleaudeau et al., 2019). Each of these studies concluded that ferruginous conditions likely dominated the Mesoproterozoic oceans with only a limited spatial extent of euxinia. It seems likely, then, that the development of regional euxinia during the Mesoproterozoic Era required special conditions such as locally high organic carbon loading (e.g., as in the ~1.1 Ga Taoudeni Basin of Mauritania; Gilleaudeau and Kah, 2015). Such conditions may have developed regionally in an ocean that was largely ferruginous where global primary productivity was perhaps limited by prolonged phosphorous biolimitation (Laakso and Schrag, 2014; Michiels et al., 2017;
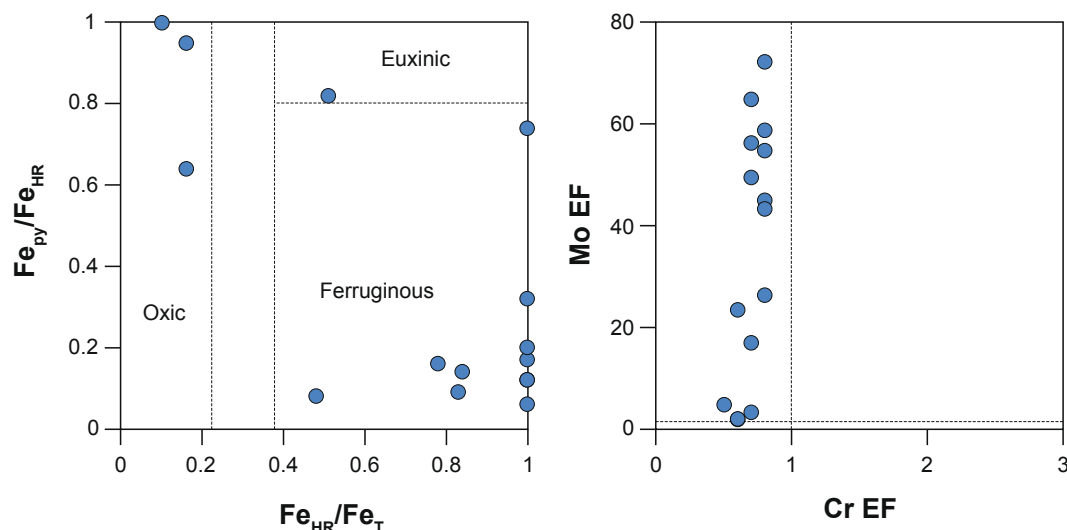

Fig. 4. Iron speciation and Mo EF vs. Cr EF cross-plots for the ~1.2 Ga Bijaygarh Shale.
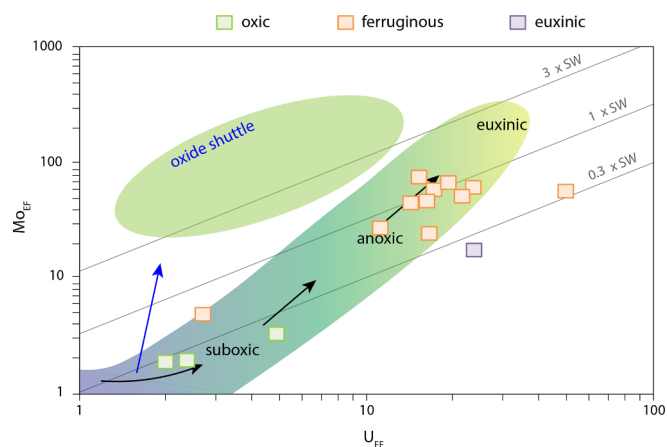
Fig. 5. Cross-plot on log-scale of our Mo EF vs. U EF data highlighting enrichment pathways based on redox conditions and the presence/absence of a local oxide shuttle. Figure based on Algeo and Tribovillard (2009) and Tribovillard et al. (2012). Dissimilar to those references, however, our EF are calculated relative to average values for the bulk upper continental crust (Rudnick and Gao 2003), not post-Archean Australian shale (PAAS).

Reinhard et al., 2017; Crockford et al., 2018; Ozaki et al., 2018). Our dominantly ferruginous iron speciation data from the Bijaygarh Shale indicate that the Vindhyan Basin may represent typical Mesoproterozoic marine conditions wherein ferruginous waters developed below the zone of wave mixing in open shelf settings.

5.2. Trace metal budget of the Mesoproterozoic ocean

The concentration of redox-sensitive trace metals (RSTMs) such as Mo, V, Cr, and U can also serve as a powerful proxy for both local and global redox conditions. RSTMs are generally soluble under oxygenated conditions yet become particle-reactive and are removed from solution in the presence of a variety of reductants. For example, under oxygenated conditions, Mo exists as the stable and conservative molybdate anion (MoO_4^{2-}). In the presence of hydrogen sulfide, however, molybdate is converted to the thiomolybdate species ($MoS_{4-x}O_x^{2-}$) and can be rapidly sequestered to sediments, particularly when $H_2S_{[aq]}$ meets or exceeds 11 μM (Erickson and Helz, 2000; Tribovillard et al., 2004; Helz et al., 2011). This process is sensitive specifically to sulfide—as opposed to general anoxia—such that high Mo concentrations in ancient sediments can be indicative of euxinic conditions during deposition (Lyons et al., 2009). Similarly, under oxygenated conditions, V exists as the soluble vanadate species but is reduced to the particle-reactive vanadyl ion or related hydroxyl species in the presence of hydrogen sulfide (Wanty and Goldhaber, 1992). Because both Mo and V are rapidly removed to sediments under euxinic conditions, their inventories in the global oceans can be related to the global extent of euxinic sedimentation and, in certain circumstances, may allow for more detailed observations based on differential patterns (Owens et al., 2016). For instance, during periods of global euxinic expansion, the Mo and V reservoirs of seawater can be drawn down (e.g., Algeo, 2004; Hetzel et al., 2009; Owens et al., 2016). By contrast, during periods of global euxinic contraction, these reservoirs can build up (e.g., Sahoo et al., 2012). Importantly, and intuitively, changes in the size of the Mo and V seawater reservoirs associated with euxinic expansion and contraction are fingerprinted by Mo and V abundances recorded in the geologic record (e.g., Scott et al., 2008, Sahoo et al., 2012).

Similar to Mo and V, Cr is soluble as chromate (CrO_4^-) under oxic conditions; however, it is efficiently reduced and removed to sediments in the presence of a variety of reductants, not just hydrogen sulfide. For example, particle-reactive $(Fe,Cr)(OH)_3$ complexes will form under ferruginous conditions (Fendorf and Li, 1996), and Cr can even be reduced and rendered insoluble under denitrifying conditions (Rue et al.,

1997). As a result, the Cr inventory of global seawater will be drawn down under conditions of widespread anoxia regardless of whether anoxia is accompanied by sulfide or ferrous iron.

In the Bijaygarh Shale, Mo is strongly enriched above crustal values (Mo EF up to 64.9), and V is mildly enriched above crustal values (V EF up to 7.0). This relationship is consistent with Vindhyan Basin waters that were replete with Mo and V. By contrast, Cr EF remains persistently low (never exceeding 0.8), and Cr is not enriched above crustal values at any point in the studied section (Figs. 3 and 4). Because we would expect Cr to be enriched in ferruginous sediments if it were available in the water column, these data suggest significant global drawdown of the seawater Cr reservoir at 1.2 Ga. This pattern of trace metal enrichment (variable Mo and V enrichment and no Cr enrichment) is consistent with the compilation of Proterozoic shale data presented by Reinhard et al. (2013). It is worth noting, however, that detrital baseline values for Cr can be variable based on terrestrial transport and weathering processes (Cole et al., 2017) and that even Phanerozoic ferruginous shales sometimes show limited Cr enrichment. Regardless, our trace metal data for the Bijaygarh Shale potentially suggest an ocean with widespread non-sulfidic anoxia, in order to drawdown the global Cr reservoir, but a restricted and variable degree of euxinia to allow for variable enrichment of Mo and V. Our data from the Bijaygarh Shale, therefore, reinforce previous interpretations of the Proterozoic trace metal record (Reinhard et al., 2013) and are broadly consistent with other proxies that suggest limited Mesoproterozoic euxinia (e.g., Gilleaudeau et al., 2019).

In addition to informing global redox conditions, differential enrichment of Mo and U in marine sediments can also be indicative of the presence or absence of a local manganese (Mn) oxide shuttle in the depositional basin (Algeo and Tribovillard, 2009). In ancient marine settings where a particulate shuttle was present, high Mo EFs are accompanied by low U EFs, and the pathway of enrichment on a cross-plot of Mo EF versus U EF deviates from typical patterns related to redox variation and water-mass restriction. In the Bijaygarh Shale, a cross-plot of Mo EF versus U EF (Fig. 5) reveals an enrichment pattern typical of increasingly anoxic (but non-euxinic) conditions in an open marine setting with no indication of a local Mn-oxide shuttle. This is broadly consistent with our iron speciation data, which indicate dominantly ferruginous conditions. The lack of a Mn-oxide shuttle is consistent with the relatively heavy δ^{98}Mo values recorded in our section (see Section 5.5) because oxide shuttling is known to introduce exceptionally light Mo-isotope values into sediments compared to coeval seawater (e.g., Ostrander et al., 2019).

5.3. Sulfur isotope constraints

The isotopic composition of sedimentary sulfides is also an important tool for deciphering past changes in ocean-atmosphere oxygenation. The soluble sulfate ion (SO_4^{2-}) is generated primarily by oxidative weathering of terrestrial sulfides and, once delivered to marine environments, can be reduced to sulfide *in situ* via microbial sulfate reduction (MSR). The resulting sulfide can then be buried in marine sediments in the form of pyrite. MSR imparts a large degree of isotopic fractionation between sulfate and sulfide (upwards of 60‰), with sulfide becoming enriched in isotopically light ^{32}S, leaving the residual sulfate pool isotopically heavy (Canfield et al., 2010; Sim et al., 2011). The magnitude of this fractionation preserved in the geologic record, however, is controlled by local sulfate availability. For example, pyrite generated under strongly sulfate-limited conditions (less than 50 μM) records little isotopic fractionation from seawater sulfate, which has an isotopic composition of approximately + 20‰ in the modern ocean (Habicht et al., 2002). By contrast, MSR under sulfate-replete conditions can produce pyrite with strongly negative isotopic compositions.

In the Bijaygarh Shale, pyrite δ^{34}S values are positive and range from +14.8 to +25.0‰, which is similar to estimates for the δ^{34}S value of Mesoproterozoic seawater sulfate (+15 to +35‰; Chu et al.,

2007). This agreement indicates that net S isotope fractionation by MSR was muted in the open Vindhyan Basin by local sulfate limitation, and also indicates that sulfate reduction was restricted to the sediments under an overall ferruginous water column. This assertion is broadly consistent with previous isotopic data from Proterozoic basins of India (Sarkar et al., 2010) and suggests a generally low sulfate Mesoproterozoic ocean. Kah et al. (2004) estimated the sulfate concentration of Mesoproterozoic seawater as between 1.5 and 4.5 mM (compared to 28 mM today); however, Fakhraee et al. (2019) recently proposed sulfate concentrations as low as 100 µM throughout the Proterozoic Eon. These levels of seawater sulfate are low enough to substantially suppress net and likely instantaneous isotopic fractionation during MSR, thus explaining the strongly positive pyrite $\delta^{34}S$ values preserved in the Bijaygarh Shale. Prolonged sulfate limitation in the Mesoproterozoic ocean was likely related to low atmospheric oxygen concentrations that potentially limited terrestrial sulfide weathering (although see Johnson et al., 2019), as well as enhanced pyrite burial in largely anoxic oceans (e.g., Gellatly and Lyons, 2005).

5.4. Nitrogen isotope constraints

Nitrogen isotopes in sedimentary organic matter can be used as an effective proxy for both metal co-factor utilization/availability during nitrogen fixation and the degree of aerobic versus anaerobic nitrogen cycling in penecontemporaneous seawater. Nitrogenase—the enzyme used in prokaryotic nitrogen fixation—most commonly relies on molybdenum as a co-factor, such that Mo-nitrogenase is expressed in all but the most Mo-limited environments (Stüeken et al., 2016). Under Mo-limited conditions, however, alternative nitrogenase enzymes using vanadium or iron as co-factors can be expressed. Anbar and Knoll (2002) hypothesized that Mo scarcity in the Mesoproterozoic ocean may have led to Mo-N co-limitation of the biosphere and thus the widespread expression of alternative nitrogenase. Zhang et al. (2014) reported laboratory experiments revealing that the expression of Mo versus alternative nitrogenase could be distinguished using N-isotopes of the resulting NH_4. In their experiments, NH_4 produced using Mo-nitrogenase had $\delta^{15}N$ values of $0 \pm 2‰$, whereas NH_4 produced using alternative nitrogenase had $\delta^{15}N$ values as low as $-7‰$.

Nitrogen isotope compositions can be modified by other processes, such as partial NH_4 assimilation, partial nitrification, partial nitrate assimilation, and the most impactful isotopic driver in the modern ocean—partial denitrification. In oxic surface waters today, nitrification is largely quantitative (producing no net isotopic effect), but denitrification occurring in oxygen minimum zones and other suboxic environments is typically incomplete. Partial denitrification preferentially removes isotopically light ^{14}N from the nitrate pool, leaving the remaining nitrate pool isotopically heavy ($\delta^{15}N = +5‰$ on average in the modern ocean; Stüeken et al., 2016). Thus, $\delta^{15}N$ values near $0 \pm 2‰$ in ancient sedimentary organic matter could be the result of a dominantly N-fixing system with limited modification from aerobic redox cycling (i.e., nitrification and denitrification), whereas strongly positive $\delta^{15}N$ values ($+3‰$ or higher) are a fingerprint for an aerobic N cycle (Stüeken et al., 2016; Koehler et al., 2017).

In the Bijaygarh Shale, all measured $\delta^{15}N$ values fall between 0 and $+3‰$ (Fig. 3). These values suggest (1) that N-fixation proceeded predominantly via Mo-nitrogenase and (2) that these open shelf waters in the Vindhyan Basin were dominantly N-fixing with little influence of an aerobic N-cycle. If alternative nitrogenase enzymes were expressed, measured $\delta^{15}N$ values would be expected to be less than $-2‰$. Additionally, if a strongly aerobic N-cycle involving nitrification and partial denitrification were operational, then measured $\delta^{15}N$ values would be expected to be greater than $+3‰$. By contrast, our data from the Bijaygarh Shale entirely fall between 0 and $+3‰$. The apparent dominance of an anaerobic N-cycle implied by these data—specifically the importance of N fixation—suggest nitrate scarcity in open Vindhyan Basin waters.

Both of these conclusions are broadly consistent with data from other Mesoproterozoic basins (Stüeken, 2013; Luo et al., 2015; Koehler et al., 2017; Cox et al., 2019). Thus far, no isotopic evidence has been found in any Archean or Proterozoic rocks for expression of alternative nitrogenase pathways (Stüeken et al., 2016), suggesting that Mo was abundant enough in the global oceans to support Mo-nitrogenase as the dominant pathway for N fixation. This possibility is also consistent with the level of Mo enrichment in Bijaygarh Shale samples (up to 34 ppm), indicating that Mo was relatively replete in the Vindhyan Basin at 1.2 Ga. Koehler et al. (2017) introduced the concept of a 'Mesoproterozoic offshore nitrate minimum' based on $\delta^{15}N$ values between -1 and $+3‰$—indicative of a largely anaerobic N-cycle—in the most distal settings of the Mesoproterozoic Bangemall Basin, Roper Basin, Belt Basin, and Xiamaling Formation. This model is in contrast to both the Paleoproterozoic and Neoproterozoic eras, where strongly positive $\delta^{15}N$ values are recorded even in distal settings. Our data from the Bijaygarh Shale are supportive of the 'offshore nitrate minimum' idea and suggest that nitrate scarcity in the open Mesoproterozoic ocean may have restricted early eukaryotes to more nutrient-replete nearshore settings (Javaux et al., 2001), thus limiting their ecological expansion until the subsequent Neoproterozoic Era.

5.5. Molybdenum isotopes as a global redox proxy

One utility of the Mo isotope proxy rests on the idea that the $\delta^{98}Mo$ value of ancient seawater has scaled to first order with levels of past global ocean oxygenation (Arnold et al., 2004). Fe-oxide and Mn-oxide minerals readily form under the presence of O_2 and possess a strong affinity for lighter-mass Mo isotopes (Goldberg et al., 2009; Wasylenki et al., 2008). Accordingly, in a well-oxygenated and oxide-rich global ocean, preferential removal of lighter-mass Mo isotopes from seawater should promote the residual enrichment of heavier-mass isotopes in seawater. This effect is seen in the modern well-oxygenated ocean: today's $\delta^{98}Mo_{seawater}$ value ($\delta^{98}Mo_{NIST+0.25} = +2.34 \pm 0.10‰$ (Nagler et al., 2014)) is much heavier than the bulk upper continental crust ($\delta^{98}Mo_{NIST+0.25} = +0.35$ to $+0.60‰$ (Willbold and Elliott, 2017)). Conversely, a primarily anoxic and thus oxide-poor global ocean would be less effective at accumulating heavier-mass isotopes in seawater. As such, comparatively light $\delta^{98}Mo_{seawater}$ values are ascribed to extensive marine anoxia—e.g., $\delta^{98}Mo$ data of up to approximately $+1.80‰$ during the Neoarchean Era (Ostrander et al., 2020 and references therein) and up to $+1.45‰$ during some Phanerozoic Oceanic Anoxic Events (Dickson, 2017).

When reconstructing past $\delta^{98}Mo_{seawater}$, it is ideal to target ancient marine shales that were deposited under euxinic conditions [summarized in Kendall et al. 2017]. Transfer of the seawater $\delta^{98}Mo$ signature to siliciclastic marine sediments occurs today in some, but not all, euxinic settings. In brief, at depth in euxinic basins such as the Black Sea, the formation of particle-reactive thiomolybdate species promotes efficient transfer of Mo from seawater into underlying sediments (particularly because local $H_2S_{[aq]}$ contents exceed 11 µM (Helz et al., 1996; Erickson and Helz, 2000)). In the case of the Black Sea, it is also a restricted basin with limited deepwater renewal, and therefore also low bottom-water Mo contents (Algeo and Lyons, 2006). This combination of factors leads to near-quantitative Mo transfer to sediments, and by extension also the effective transfer of the seawater Mo-isotope signature (Neubert et al. 2008). Such behavior is also observed in the deep portions of modern restricted Kyllaren fjord (Noordmann et al., 2015), as well as in Lake Rogoznica (Bura-Nakic et al., 2018)).

Our shales from the Vindhyan Basin were deposited according to Fe-speciation data under locally ferruginous conditions (Fig. 4)—not the ideal euxinic conditions for capturing $\delta^{98}Mo_{seawater}$ signatures. Sequestration of Mo in shales from the Vindhyan Basin does seem coupled to some extent to local sulfide availability, evident in the general correlation between increasing sedimentary Mo and S abundances ($R^2 = 0.70$). However, given the generally ferruginous Fe-speciation signal of our shale samples, it is unlikely that local bottom-water H_2S

abundances were sufficiently high to promote near-quantitative transfer of Mo to the original sediments. In modern marine settings with low or variable bottom-water H_2S contents, or in locations where H_2S is restricted to sediment porewaters, non-quantitative transfer of Mo to sediments results in sedimentary $\delta^{98}Mo$ that are highly variable but always lighter than the overlying seawater signature (e.g., due to the formation of intermediate thiomolybdates (Neubert et al. 2008), organic matter (King et al. 2018), and/or Fe-Mo-S minerals (Helz et al. 2011)). By analogy, our measured $\delta^{98}Mo$ from shales of the Vindhyan Basin (up to $\delta^{98}Mo = +1.18 \pm 0.12‰$) are probably also not representative of the ancient seawater signature and instead are most likely skewed toward isotopically lighter values. It is worth mentioning here, however, that in a Mesoproterozoic ocean with lower Mo availability (Scott et al. 2008; Gilleaudeau and Kah, 2013; Reinhard et al. 2013), quantitative transfer of Mo from seawater into sediments may have been more likely, and perhaps even took place in marine settings where H_2S was limited to sediment pore waters (discussed in Ostrander et al. 2020). In either scenario, our heaviest $\delta^{98}Mo$ value still serves as a conservative estimate for the 1.2 Ga seawater $\delta^{98}Mo$ signature, and seawater, if anything, was heavier.

Although our shale $\delta^{98}Mo$ data may not accurately track the 1.2 Ga seawater signature, these values may provide a qualitative perspective on the scale of global ocean oxygenation at that time. Specifically, our $\delta^{98}Mo$ from ancient shales deposited under locally ferruginous conditions can be compared to those found in other Proterozoic shales deposited under the same conditions. When this comparison is made, our maximum $\delta^{98}Mo$ value from the Vindhyan Basin of $+1.18 \pm 0.12‰$ is indistinguishable from those found in other shales deposited under ferruginous conditions throughout the Proterozoic—e.g., $+1.03 \pm 0.18‰$ in the 1.7 Ga Wollogorang Formation from northern Australia (Kendall et al., 2009), $+0.99 \pm 0.15‰$ in the 1.4 Ga Xiamaling Formation from north China (although it is worth noting that some of these shale samples are thought to have been deposited in a restricted basin; Diamond et al., 2018), and $+0.83 \pm 0.27‰$ in the 0.75 Ga Chuar Group from the southwestern United States (Dahl et al., 2011) (Fig. 6).

The likeness of our 1.2 Ga shale $\delta^{98}Mo$ to those found in 1.7 Ga, 1.4 Ga, and 0.75 Ga shales may imply that $\delta^{98}Mo_{seawater}$ was comparable at these times, and by inference so too were global marine redox conditions. Alternatively, this likeness may be a coincidence. As we discussed earlier, shales deposited today under non-euxinic conditions are particularly poor at capturing seawater $\delta^{98}Mo$. It is therefore also possible that some or none of these ancient shales captured $\delta^{98}Mo_{seawater}$. This alternate scenario would leave open the possibility of variable $\delta^{98}Mo_{seawater}$ at these times, and by inference also variable global marine redox conditions. This scenario also leaves open the possibility of a very heavy $\delta^{98}Mo_{seawater}$ at times during the Proterozoic Eon, which would indicate a well-oxygenated global ocean. Importantly, however, consistently muted Cr and Mo abundances in shales deposited throughout the Proterozoic Eon, including the Bijaygarh Shale (see Fig. 6), add credence to the idea of a Proterozoic ocean with generally low levels of free oxygen (Reinhard et al., 2013).

6. Conclusions

In this study, we present a new, multi-proxy geochemical dataset from the ~1.2 Ga Bijaygarh Shale, Vindhyan Basin, India. We use total organic carbon, iron speciation, and trace metal abundances, as well as sulfur, nitrogen, and molybdenum isotope compositions to provide new constraints on the oxygenation history of Mesoproterozoic seawater. In summary, our dataset captures a snapshot of conditions that may have been typical of the Mesoproterozoic oceans: (1) ferruginous waters below the zone of wave mixing in open shelf environments; (2) muted enrichment of metals sensitive to anoxia (Cr) and variable enrichment of metals sensitive to euxinia (Mo, V), indicating a largely anoxic (ferruginous) ocean with only limited extent of euxinia; (3) general sulfate limitation; and (4) nitrogen fixation via Mo-nitrogenase and a
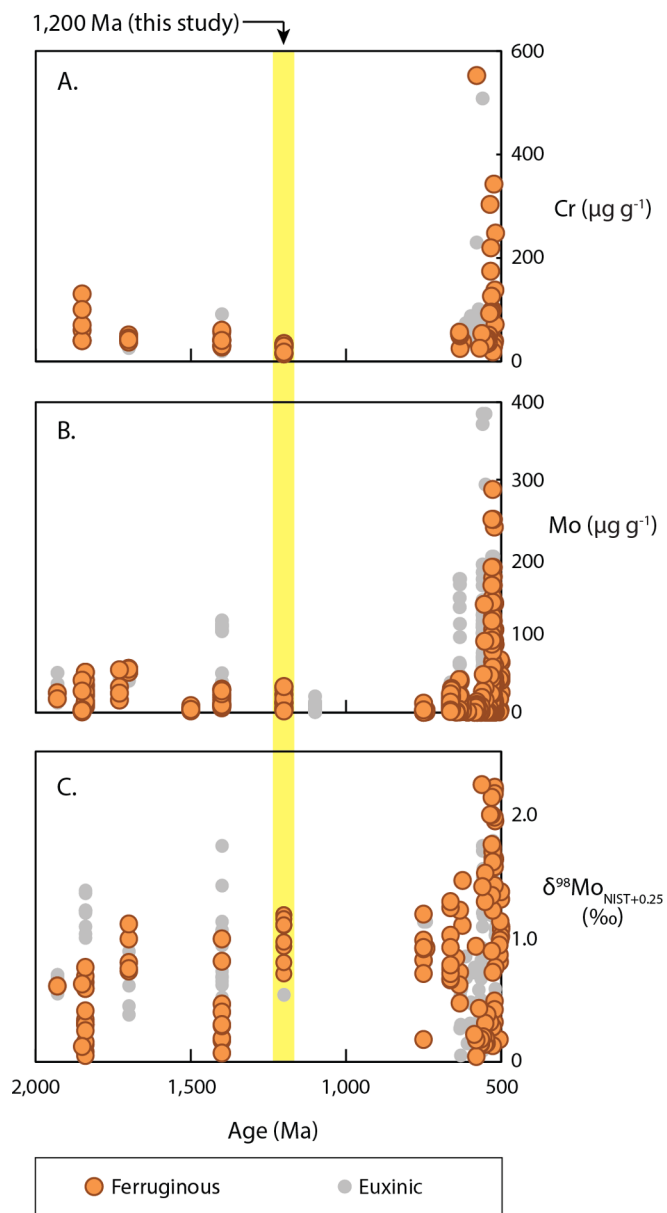

Fig. 6. Compilation of all published [Mo], [Cr], and Mo-isotope data for successions spanning 2.0 to 0.5 Ga. Samples are separated based on local depositional redox conditions (as determined by published iron speciation data) and samples from this study are highlighted in yellow. (For interpretation of the references to colour in this figure legend, the reader is referred to the web version of this article.)

dominantly anaerobic nitrogen cycle in offshore waters. In addition, this study provides the first molybdenum isotope data from unambiguously marine shale deposited between 1.4 and 0.75 Ga. $\delta^{98}Mo$ values up to $+1.18 \pm 0.12‰$ are comparable to both older and younger Proterozoic successions and are consistent with redox trends recorded globally in Mesoproterozoic strata. Ultimately, our data from the Vindhyan Basin fill an important gap in the Proterozoic record of ocean oxygenation and provide critical constraints on the environmental conditions that accompanied early eukaryotic evolution.

Declaration of Competing Interest

The authors declare that they have no known competing financial interests or personal relationships that could have appeared to influence the work reported in this paper.

Acknowledgements

References

Algeo, T.J., 2004. Can marine anoxic events draw down the trace element inventory of seawater? Geology 32, 1057–1060.

Algeo, T.J., Lyons, T.W., 2006. Mo-total organic carbon covariation in modern anoxic marine environments: implications for analysis of paleoredox and paleohydrographic conditions. Paleoceanography 21 (PA1016), 1–23.

Algeo, T.J., Tribovillard, N., 2009. Environmental analysis of paleoceanographic systems based on molybdenum-uranium covariation. Chem. Geol. 268, 211–225.

Anbar, A.D., Knoll, A.H., 2002. Proterozoic ocean chemistry and evolution: a bioinorganic bridge? Science 297, 1137–1142.

Anderson, T.F., Raiswell, R., 2004. Sources and mechanisms for the enrichment of highly reactive iron in euxinic Black Sea sediments. Am. J. Sci. 304, 203–233.

Arnold, G.L., Anbar, A.D., Barling, J., Lyons, T.W., 2004. Molybdenum isotope evidence for widespread anoxia in mid-Proterozoic oceans. Science 304, 87–90.

Azmi, R.J., 1998. Discovery of Lower Cambrian small shelly fossils and brachiopods from the Lower Vindhyan of the Son Valley, Central India. J. Geol. Soc. India 52, 381–389.

Banerjee, I., 1982. The Vindhyan tidal sea. In: Valdiya, K.S., Bhatia, S.B., Gaur, V.K. (Eds.), Geology of Vindhyachal. Hindusthan Publishing Corporation, Delhi.

Banerjee, S., Dutta, S., Paikaray, S., Mann, U., 2006. Stratigraphy, sedimentology, and bulk organic geochemistry of black shales from the Proterozoic Vindhyan Supergroup (central India). J. Earth Syst. Sci. 115, 37–47.

Barling, J., Arnold, G.L., Anbar, A.D., 2001. Natural mass-dependent variations in the isotopic composition of molybdenum. Earth Planet. Sci. Lett. 193, 447–457.

Beghin, J., Guilbaud, R., Poulton, S.W., Gueneli, N., Brocks, J.J., Storme, J.Y., Blanpied, C., Javaux, E.J., 2017. A palaeoecological model for the late Mesoproterozoic-early Neoproterozoic Atar/El Mreiti Group, Taoudeni Basin, Mauritania, northwestern Africa. Precambr. Res. 299, 1–14.

Bickford, M.E., Mishra, M., Mueller, P.A., Kamenov, G.D., Schieber, J., Basu, A., 2017. U-Pb age of Hf isotope compositions of magmatic zircons from a rhyolite flow in the Porcellanite Formation in the Vindhyan Supergroup, Son Valley (India): implications for its tectonic significance. J. Geol. 125, 367–379.

Blumenberg, M., Thiel, V., Riegel, W., Kah, L.C., Reitner, J., 2012. Biomarkers of black shales formed by microbial mats, Late Mesoproterozoic (1.1 Ga) Taoudeni Basin, Mauritania. Precambrian Res. 196–197, 113–127.

Bose, P.K., Sarkar, S., Chakrabarty, S., Banerjee, S., 2001. Overview of the Meso- to Neoproterozoic evolution of the Vindhyan Basin, central India. Sed. Geol. 141–142, 395–419.

Brocks, J.J., Love, G.D., Summons, R.E., Knoll, A.H., Logan, G.A., Bowden, S.A., 2005. Biomarker evidence for green and purple sulphur bacteria in a stratified Palaeoproterozoic sea. Nature 437, 866–870.

Bura-Nakic, E., Andersen, M.B., Archer, C., de Souza, G.F., Margus, M., Vance, D., 2018. Coupled Mo-U abundances and isotopes in a small marine euxinic basin: constraints on processes in euxinic basins. Geochim. Cosmochim. Acta 222, 212–229.

Canfield, D.E., Farquhar, J., Zerkle, A.L., 2010. High isotope fractionations during sulfate reduction in a low-sulfate euxinic ocean analog. Geology 38, 415–418.

Canfield, D., Lyons, T., Raiswell, R., 1996. A model for iron deposition to euxinic Black Sea sediments. Am. J. Sci. 296, 818–834.

Canfield, D.E., Raiswell, R., Westrich, J.T., Reaves, C.M., Berner, R.A., 1986. The use of chromium reduction in the analysis of reduced inorganic sulfur in sediments and shales. Chem. Geol. 54, 149–155.

Chakraborty, C., 1995. Gutter casts from the Proterozoic Bijaygarh Shale Formation, India: their implication for storm-induced circulation in shelf settings. Geol. J. 30, 69–78.

Chakraborty, C., 2006. Proterozoic intracontinental basin: the Vindhyan example. J. Earth Syst. Sci. 115, 3–22.

Chakraborty, C., Bose, P.K., 1990. Internal structures of sandwaves in a tide-storm interactive system: Proterozoic Lower Quartzite Formation, India. Sed. Geol. 67, 133–142.

Chanda, S.K., Bhattacharya, A., 1982. Vindhyan sedimentation and paleogeography: post-Auden developments. In: Valdiya, K.S., Bhatia, S.B., Gaur, V.K. (Eds.), Geology of Vindhyachal. Hindusthan Publishing Corporation, Delhi.

Chu, X., Zhang, T., Zhang, Q., Lyons, T.W., 2007. Sulfur and carbon isotope records from 1700 to 800 Ma carbonates of the Jixian section, northern China: Implications for secular isotope variations in Proterozoic seawater and relationships to global supercontinent events. Geochim. Cosmochim. Acta 71, 4668–4692.

Cole, D.B., Reinhard, C.T., Wang, X., Gueguen, B., Halverson, G.P., Gibson, T., Hodgskiss, M.S.W., McKenzie, N.R., Lyons, T.W., Planavsky, N.J., 2016. A shale-hosted Cr isotope record of low atmospheric oxygen during the Proterozoic. Geology 44, 555–558.

Cole, D.B., Zhang, S., Planavsky, N.J., 2017. A new estimate of detrital redox-sensitive metal concentrations and variability in fluxes to marine sediments. Geochim. Cosmochim. Acta 215, 337–353.

Cox, G.M., Jarrett, A., Edwards, D., Crockford, P.W., Halverson, G.P., Collins, A.S., Poirier, A., Li, Z.X., 2016. Basin redox and primary productivity with the Mesoproterozoic Roper Seaway. Chem. Geol. 440, 101–114.

Cox, G.M., Sansjofre, P., Blades, M.L., Farkas, J., Collins, A.S., 2019. Dynamic interaction between basin redox and the biogeochemical nitrogen cycle in an unconventional Proterozoic petroleum system. Sci. Rep. 9, 5200.

Crockford, P.W., Hayles, J.A., Bao, H., Planavsky, N.J., Bekker, A., Fralick, P.W., Halverson, G.P., Bui, T.H., Peng, Y., Wing, B.A., 2018. Triple oxygen isotope evidence for limited mid-Proterozoic primary productivity. Nature 559, 613–616.

Dahl, T.W., Canfield, D.E., Rosing, M.T., Frei, R.E., Gordon, G.W., Knoll, A.H., Anbar, A.D., 2011. Molybdenum evidence for expansive sulfidic water masses in ~750 Ma oceans. Earth Planet. Sci. Lett. 311, 264–274.

De, C., 2006. Ediacara fossil assemblage in the upper Vindhyans of central India and its significance. J. Asian Earth Sci. 27, 660–683.

Diamond, C.W., Planavsky, N.J., Wang, C., Lyons, T.W., 2018. What the ~1.4 Xiamaling Formation can and cannot tell us about the mid-Proterozoic ocean. Geobiology. https://doi.org/10.1111/gbi.12282.

Diamond, C.W., Lyons, T.W., 2018. Mid-Proterozoic redox evolution and the possibility of transient oxygenation events. Emerg. Topics Life Sci. 2, 235–245.

Dickson, A.J., 2017. A molybdenum-isotope perspective on Phanerozoic deoxygenation events. Nat. Geosci. 10, 721–726.

Doyle, K.A., Poulton, S.W., Newton, R.J., Podkovyrov, V.N., Bekker, A., 2018. Shallow water anoxia in the Mesoproterozoic ocean: evidence from the Bashkir Meganticlinorium, Southern Urals. Precambr. Res. 317, 196–210.

Erickson, B.E., Helz, G.R., 2000. Molybdenum (VI) speciation in sulfidic waters: stability and lability of thiomolybdates. Geochim. Cosmochim. Acta 64, 1149–1158.

Fakhraee, M., Hancisse, O., Canfield, D.E., Crowe, S.A., Katsev, S., 2019. Proterozoic seawater sulfate scarcity and the evolution of ocean-atmosphere chemistry. Nat. Geosci. 12, 375–380.

Fendorf, S.E., Li, G., 1996. Kinetics of chromate reduction by ferrous iron. Environ. Sci. Technol. 30, 1614–1617.

Gellatly, A.M., Lyons, T.W., 2005. Trace sulfate in mid-Proterozoic carbonates and the sulfur isotope record of biospheric evolution. Geochim. Cosmochim. Acta 69, 3813–3829.

Gilleaudeau, G.J., Frei, R., Kaufman, A.J., Kah, L.C., Azmy, K., Bartley, J.K., Chernyavskiy, P., Knoll, A.H., 2016. Oxygenation of the mid-Proterozoic atmosphere: clues from chromium isotopes in carbonates. Geochem. Perspectives Lett. 2, 178–187.

Gilleaudeau, G.J., Kah, L.C., 2013. Oceanic molybdenum drawdown by epeiric sea expansion in the Mesoproterozoic. Chem. Geol. 356, 21–37.

Gilleaudeau, G.J., Kah, L.C., 2015. Heterogeneous redox conditions and a shallow chemocline in the Mesoproterozoic ocean: evidence from carbon-sulfur-iron relationships. Precambr. Res. 257, 94–108.

Gilleaudeau, G.J., Romaniello, S.J., Luo, G., Kaufman, A.J., Zhang, F., Klaebe, R.M., Kah, L.C., Azmy, K., Bartley, J.K., Zheng, W., Knoll, A.H., Anbar, A.D., 2019. Uranium isotope evidence for limited euxinia in mid-Proterozoic oceans. Earth Planet. Sci. Lett. 521, 150–157.

Gilleaudeau, G.J., Sahoo, S.K., Kah, L.C., Henderson, M.A., Kaufman, A.J., 2018. Proterozoic carbonates of the Vindhyan Basin, India: chemostratigraphy and diagenesis. Gondwana Res. 57, 10–25.

Goldberg, T., Archer, C., Vance, D., Poulton, S.W., 2009. Mo isotope fractionation during adsorption to Fe (oxyhydr)oxides. Geochim. Cosmochim. Acta 73, 6502–6516.

Goldberg, T., Gordon, G., Izon, G., Archer, C., Pearce, C.R., McManus, J., Anbar, A.D., Rehkämper, M., 2013. Resolution of inter-laboratory discrepancies in Mo isotope data: an intercalibration. J. Anal. At. Spectrom. 28, 724–735.

Gopalan, K., Kumar, A., Kumar, S., Vijayagopal, B., 2013. Depositional history of the Upper Vindhyan succession, central India: time constraints from Pb-Pb isochron ages of its carbonate components. Precambr. Res. 233, 108–117.

Gregory, L.C., Meert, J.G., Pradhan, V., Pandit, M.K., Tamrat, E., Malone, S.J., 2006. A paleomagnetic and geochronologic study of the Majhgawan kimberlite, India: implications for the age of the Upper Vindhyan Supergroup. Precambr. Res. 149, 65–75.

Habicht, K.S., Gade, M., Thamdrup, B., Berg, P., Canfield, D.E., 2002. Calibration of sulfate levels in the Archean Ocean. Science 298, 2372–2374.

Hardisty, D.S., Lu, Z., Bekker, A., Diamond, C.W., Gill, B.C., Jiang, G., Kah, L.C., Knoll, A.H., Loyd, S.J., Osburn, M.R., Planavsky, N.J., Wang, C., Zhou, X., Lyons, T.W., 2017. Perspectives on Proterozoic surface ocean redox from iodine contents in ancient and recent carbonate. Earth Planet. Sci. Lett. 463, 159–170.

Hardisty, D.S., Lyons, T.W., Riedinger, N., Isson, T.T., Owens, J.D., Aller, R.C., Rye, D.M., Planavsky, N.J., Reinhard, C.T., Gill, B.C., Masterson, A.L., Asael, D., Johnston, D.T., 2018. An evaluation of sedimentary molybdenum and iron as proxies for pore fluid paleoredox conditions. Am. J. Sci. 318, 527–556.

Helz, G.R., Bura-Nakic, E., Mikac, N., Ciglenecki, I., 2011. New model for molybdenum behavior in euxinic waters. Chem. Geol. 284, 323–332.

Helz, G.R., Miller, C.V., Charnock, J.M., Mosselmans, J.F.W., Pattrick, R.A.D., Garner, C.D., Vaughan, D.J., 1996. Mechanism of molybdenum removal from the sea and its concentration in black shales: EXAFS evidence. Geochim. Cosmochim. Acta 60, 3631–3642.

Hetzel, A., Bottcher, M.E., Wortmann, U.G., Brumsack, H.J., 2009. Paleo-redox conditions during OAE 2 reflected in Demerara Rise sediment geochemistry (ODP Leg 2017). Palaeogeogr., Palaeoclimatol., Palaeogeogr. 273, 302–328.

Javaux, E.J., Knoll, A.H., Walter, M.R., 2001. Morphological and ecological complexity in early eukaryotic ecosystems. Nature 412, 66–69.

Johnson, A.C., Romaniello, S.J., Reinhard, C.T., Gregory, D.D., Garcia-Robledo, E.,

Revsbech, N.P., Canfield, D.E., Lyons, T.W., Anbar, A.D., 2019. Experimental determination of pyrite and molybdenite oxidation kinetics at nanomolar oxygen concentrations. Geochim. Cosmochim. Acta 249, 160–172.

Kah, L.C., Lyons, T.W., Frank, T.D., 2004. Low marine sulphate and protracted oxygenation of the Proterozoic biosphere. Nature 431, 834–838.

Kendall, B., Creaser, R.A., Gordon, G.W., Anbar, A.D., 2009. Re-Os and Mo isotope systematics of black shales from the Middle Proterozoic Velkerri and Wollogorang Formations, McArthur Basin, northern Australia. Geochim. Cosmochim. Acta 73, 2534–2558.

Kendall, B., Dahl, T.W., Anbar, A.D., 2017. The stable isotope geochemistry of molybdenum. Rev. Mineral. Geochem. 82, 683–732.

Kendall, B., Gordon, G.W., Poulton, S.W., Anbar, A.D., 2011. Molybdenum isotope constraints on the extent of late Paleoproterozoic ocean euxinia. Earth Planet. Sci. Lett. 307, 450–460.

Kendall, B., Reinhard, C.T., Lyons, T.W., Kaufman, A.J., Poulton, S.W., Anbar, A.D., 2010. Pervasive oxygenation along late Archaean ocean margins. Nat. Geosci. 3, 647–652.

King, E.K., Perakis, S.S., Pett-Ridge, J.C., 2018. Molybdenum isotope fractionation during adsorption to organic matter. Geochim. Cosmochim. Acta 222, 584–598.

Koehler, M.C., Stüeken, E.E., Kipp, M.A., Buick, R., Knoll, A.H., 2017. Spatial and temporal trends in Precambrian nitrogen cycling: a Mesoproterozoic offshore nitrate minimum. Geochim. Cosmochim. Acta 198, 315–337.

Laakso, T.A., Schrag, D.P., 2014. Regulation of atmospheric oxygen during the Proterozoic. Earth Planet. Sci. Lett. 388, 81–91.

Luo, G., Hallmann, C., Xie, S., Ruan, X., Summons, R.E., 2015. Comparative mirobial diversity and redox environments of black shale and stromatolite facies in the Mesoproterozoic Xiamaling Formation. Geochim. Cosmochim. Acta 151, 150–167.

Lyons, T.W., Anbar, A.D., Severmann, S., Scott, C., Gill, B.C., 2009. Tracking euxinia in the ancient ocean: a multiproxy perspective and Proterozoic case study. Ann. Rev. Earth Planet. Sci. 37, 507–534.

Lyons, T.W., Severmann, S., 2006. A critical look at iron paleoredox proxies: new insights from modern euxinic marine basins. Geochim. Cosmochim. Acta 70, 5698–5722.

Maharjan, D., Jiang, G., Peng, Y., Henry, R.A., 2018. Paired carbonate-organic carbon and nitrogen isotope variations in Lower Mississippian strata of the southern Great Basin, western United States. Palaeogeogr. Palaeoclimatol. Palaeoecol. 490, 462–472.

Malone, S.J., Meert, J.G., Banerjee, D.M., Pandit, M.K., Tamrat, E., Kamenov, G.D., Pradhan, V.R., Sohl, L.E., 2008. Paleomagnetism and detrital zircon geochronology of the Upper Vindhyan sequence, Son Valley and Rajasthan, India: a ca. 1000 Ma closure age for the Purana basins? Precambr. Res. 164, 137–159.

März, C., Poulton, S.W., Beckmann, B., Küster, K., Wagner, T., Kasten, S., 2008. Redox sensitivity of P cycling during marine black shale formation: dynamics of sulfidic and anoxic, non-sulfidic bottom waters. Geochim. Cosmochim. Acta 72, 3703–3717.

Mazumder, R., Bose, P.K., Sarkar, S., 2000. A commentary on the tectono-sedimentary record of the pre-2.0 Ga continental growth of India vis-à-vis a possible pre-Gondwana Afro-Indian supercontinent. J. Afr. Earth Sc. 30, 201–217.

McKenzie, N.R., Hughes, N.C., Myrow, P.M., Xiao, S., Sharma, M., 2011. Corrrelation of Precambrian-Cambrian sedimentary successions across northern India and the utility of isotopic signatures of Himalayan lithotectonic zones. Earth Planet. Sci. Lett. 312, 471–483.

McKenzie, N.R., Hughes, N.C., Myrow, P.M., Banerjee, D.M., Deb, M., Planavsky, N.J., 2013. New age constraints for the Proterozoic Aravalli-Delhi successions of India and their implications. Precambr. Res. 238, 120–128.

Michiels, C.C., Darchambeau, F., Roland, F.A.E., Morana, C., Lliros, M., Garcia-Armisen, T., Thamdrup, B., Borges, A.V., Canfield, D.E., Servais, P., Descy, J.P., Crowe, S.A., 2017. Iron-dependent nitrogen cycling in a ferruginous lake and the nutrient status of the Proterozoic oceans. Nat. Geosci. 10, 217–221.

Nagler, T.F., Anbar, A.D., Archer, C., Goldberg, T., Gordon, G.W., Greber, N.D., Siebert, S., Sohrin, Y., Vance, D., 2014. Proposal for an international molybdenum isotope measurement standard and data representation. Geostand. Geoanal. Res. https://doi.org/10.1111/j.1751-908X.2013.00275.x.

Neubert, N., Nägler, T.F., Böttcher, M.E., 2008. Sulfidity controls molybdenum isotope fractionation into euxinic sediments: evidence from the modern Black Sea. Geology 36, 775–778.

Nguyen, K., Love, G.D., Zumberge, J.A., Kelly, A.E., Owens, J.D., Rohrssen, M.K., Bates, S.M., Cai, C., Lyons, T.W., 2019. Absence of biomarker evidence for early eukaryotic life from the Mesoproterozoic Roper Group: Searching across a marine redox gradient in mid-Proterozoic habitability. Geobiology 17, 247–260.

Noordmann, J., Weyer, S., Montoya-Pino, C., Dellwig, O., Neubert, N., Eckert, S., Paetzel, M., Bottcher, M.E., 2015. Uranium and molybdenum isotope systematics in modern euxinic basins: case studies from the central Baltic Sea and the Kyllaren fjord (Norway). Chem. Geol. 396, 182–195.

Ostrander, C.M., Sahoo, S.K., Kendall, B., Jiang, G., Planavsky, N.J., Lyons, T.W., Nielsen, S.G., Owens, J.D., Gordon, G.W., Romaniello, S.J., Anbar, A.D., 2019. Multiple negative molybdenum isotope excursions in the Doushantuo Formation (South China) fingerprint complex redox-related processes in the Ediacaran Nanhua Basin. Geochim. Cosmochim. Acta 261, 191–209.

Ostrander, C.M., Kendall, B., Olson, S.L., Lyons, T.W., Gordon, G.W., Romaniello, S.J., Zheng, W., Reinhard, C.T., Roy, M., Anbar, A.D., 2020. An expanded shale $\delta^{98}Mo$ record permits recurrent shallow marine oxygenation during the Neoarchean. Chem. Geol. 532, 119391.

Owens, J.D., Reinhard, C.T., Rohrssen, M., Love, G.D., Lyons, T.W., 2016. Empirical links between trace metal cycling and marine microbial ecology during a large perturbation to Earth's carbon cycle. Earth Planet. Sci. Lett. 449, 407–417.

Ozaki, K., Reinhard, C.T., Tajika, E., 2018. A sluggish mid-Proterozoic biosphere and its effect on Earth's redox balance. Geobiology. https://doi.org/10.1111/gbi.12317.

Planavsky, N.J., McGoldrick, P., Scott, C.T., Li, C., Reinhard, C.T., Kelly, A.E., Chu, X., Bekker, A., Love, G.D., Lyons, T.W., 2011. Widespread iron-rich conditions in the mid-Proterozoic ocean. Nature 477, 448–451.

Planavsky, N.J., Reinhard, C.T., Wang, X., Thomson, D., McGoldrick, P., Rainbird, R.H., Johnson, T., Fischer, W.W., Lyons, T.W., 2014. Low mid-Proterozoic atmospheric oxygen levels and the delayed rise of animals. Science 346, 635–638.

Planavsky, N.J., Slack, J.F., Cannon, W.F., O'Connell, B., Isson, T.T., Asael, D., Jackson, J.C., Hardisty, D.S., Lyons, T.W., Bekker, A., 2018. Evidence for episodic oxygenation in a weakly redox-buffered deep mid-Proterozoic ocean. Chem. Geol. 483, 581–594.

Poulton, S.W., Canfield, D.E., 2005. Development of a sequential extraction procedure for iron: implications for iron partitioning in continentally derived particulates. Chem. Geol. 214, 209–221.

Poulton, S.W., Canfield, D.E., 2011. Ferruginous conditions: A dominant feature of the ocean through Earth's history. Elements 7, 107–112.

Poulton, S.W., Fralick, P.W., Canfield, D.E., 2004. The transition to a sulphidic ocean ~1.84 billion years ago. Nature 431, 173–177.

Prasad, B.R., Rao, V.V., 2006. Deep seismic reflection study over the Vindhyans of Rajasthan: implications for geophysical setting of the basin. J. Earth Syst. Sci. 115, 135–147.

Quasim, M.A., Ahmad, A.H.M., 2015. Petrofacies and tectonic setup of Kaimur Group of rocks, Son Valley, India. Palaeobotanist 64, 1–11.

Raiswell, R., Canfield, D.E., 1998. Sources of iron for pyrite formation in marine sediments. Am. J. Sci. 298, 219–245.

Ramakrishnan, M., Vaidyanadhan, R., 2008. Geology of India. Geological Society of India.

Rasmussen, B., Bose, P.K., Sarkar, S., Banerjee, S., Fletcher, I.R., McNaughton, N.J., 2002. 1.6 Ga U-Pb zircon age for the Chorhat Sandstone, lower Vindhyan, India: possible implications for the early evolution of animals. Geology 30, 103–106.

Ray, J.S., 2006. Age of the Vindhyan Supergroup: a review of recent findings. J. Earth Syst. Sci. 115, 149–160.

Ray, J.S., Martin, M.W., Veizer, J., Bowring, S.A., 2002. U-Pb zircon dating and Sr isotope systematics of the Vindhyan Supergroup, India. Geology 30, 131–134.

Ray, J.S., Veizer, J., Davis, W.J., 2003. C, O, Sr and Pb isotope systematics of carbonate sequences of the Vindhyan Supergroup, India: age, diagenesis, correlations and implications for global events. Precambr. Res. 121, 103–140.

Reinhard, C.T., Planavsky, N.J., Gill, B.C., Ozaki, K., Robbins, L.J., Lyons, T.W., Fischer, W.W., Wang, C., Cole, D.B., Konhauser, K.O., 2017. Evolution of the global phosphorus cycle. Nature 541, 386–389.

Reinhard, C.T., Planavsky, N.J., Robbins, L.J., Partin, C.A., Gill, B.C., Lalonde, S.V., Bekker, A., Konhauser, K.O., Lyons, T.W., 2013. Proterozoic ocean redox and biogeochemical stasis. Proc. Natl. Acad. Sci. U.S.A. 110, 5357–5362.

Rudnick, R.L., Gao, S., 2003. Composition of the continental crust. Treat. Geochem. 3.

Rue, E.L., Smith, G.J., Cutter, G.A., Bruland, K.W., 1997. The response of trace element redox couples to suboxic conditions in the water column. Deep Sea Res. Part I 44, 113–134.

Sahoo, S.K., Planavsky, N.J., Kendall, B., Wang, X., Shi, X., Scott, C., Anbar, A.D., Lyons, T.W., Jiang, G., 2012. Ocean oxygenation in the wake of the Marinoan glaciation. Nature 489, 546–549.

Sarkar, A., Chakraborty, P.P., Mishra, B., Bera, M.K., Sanyal, P., Paul, S., 2010. Mesoproterozoic sulphidic ocean, delayed oxygenation and evolution of early life: sulphur isotope clues from Indian Proterozoic basins. Geol. Mag. 147, 206–218.

Scott, C., Lyons, T.W., Bekker, A., Shen, Y., Poulton, S.W., Chu, X., Anbar, A.D., 2008. Tracing the stepwise oxygenation of the Proterozoic ocean. Nature 452, 456–459.

Sheen, A.I., Kendall, B., Reinhard, C.T., Creaser, R.A., Lyons, T.W., Bekker, A., Poulton, S.W., Anbar, A.D., 2018. A model for the oceanic mass balance of rhenium and implications for the extent of Proterozoic ocean anoxia. Geochim. Cosmochim. Acta 227, 75–95.

Shen, Y., Canfield, D.E., Knoll, A.H., 2002. Middle Proterozoic ocean chemistry: evidence from the McArthur Basin, northern Australia. Am. J. Sci. 302, 81–109.

Shen, Y., Knoll, A.H., Walter, M.R., 2003. Evidence for low sulphate and anoxia in a mid-Proterozoic marine basin. Nature 423, 632–635.

Sim, M.S., Bosak, T., Ono, S., 2011. Large sulfur isotope fractionation does not require disproportionation. Science 333, 74–77.

Singh, A.K., Chakraborty, P.P., Sarkar, S., 2018. Redox structure of the Vindhyan hydrosphere: clues from total organic carbon, transition metal (Mo, Cr) concentrations and stable isotope ($\delta^{13}C$) chemistry. Curr. Sci. 115, 1334–1341.

Sperling, E.A., Rooney, A.D., Hays, L., Sergeev, V.N., Vorob'eva, N.G., Sergeeva, N.D., Selby, D., Johnston, D.T., Knoll, A.H., 2014. Redox heterogeneity of subsurface waters in the Mesoproterozoic ocean. Geobiology 12, 373–386.

Sperling, E.A., Wolock, C.J., Morgan, A.S., Gill, B.C., Kunzmann, M., Halverson, G.P., Macdonald, F.A., Knoll, A.H., Johnston, D.T., 2015. Statistical analysis of iron geochemical data suggests limited late Proterozoic oxygenation. Nature 523, 451–454.

Stüeken, E.E., 2013. A test of the nitrogen-limitation hypothesis for retarded eukaryote radiation: nitrogen isotopes across a Mesoproterozoic basinal profile. Geochim. Cosmochim. Acta 120, 121–139.

Stüeken, E.E., Bellefroid, E., Prave, A.R., Asael, D., Planavsky, N., Lyons, T., 2017. Not so non-marine? revisiting the Stoer Group and the Mesoproterozoic biosphere. Geochem. Perspectives Lett. 3, 221–229.

Stüeken, E.E., Kipp, M.A., Koehler, M.C., Buick, R., 2016. The evolution of Earth's biogeochemical nitrogen cycle. Earth Sci. Rev. 160, 220–239.

Tribovillard, N., Riboulleau, A., Lyons, T.W., Baudin, F., 2004. Enhanced trapping of molybdenum by sulfurized organic matter of marine origin in Mesozoic limestones and shales. Chem. Geol. 213, 385–401.

Tribovillard, N., Algeo, T.J., Baudin, F., Riboulleau, A., 2012. Analysis of marine environmental conditions based on molybdenum-uranium covariation—applications to Mesozoic paleoceanography. Chem. Geol. 324–325, 46–58.

Tripathy, G.R., Singh, S.K., 2015. Re-Os depositional age for black shales from the Kaimur Group, Upper Vindhyan, India. Chem. Geol. 413, 63–72.

Turner, C.C., Meert, J.G., Pandit, M.K., Kamenov, G.D., 2014. A detrital zircon U-Pb and

Hf isotopic transect across the Son Valley sector of the Vindhyan Basin, India: implications for basin evolution and paleogeography. Gondwana Res. 26, 348–364.

Wanty, R.B., Goldhaber, M.B., 1992. Thermodynamics and kinetics of reactions involving vanadium in natural systems: accumulation of vanadium in sedimentary rocks. Geochim. Cosmochim. Acta 56, 1471–1483.

Wasylenki, L.E., Rolfe, B.A., Weeks, C.L., Spiro, T.G., Anbar, A.D., 2008. Experimental investigation of the effects of temperature and ionic strength on Mo isotope fractionatiom during adsorption to manganese oxides. Geochim. Cosmochim. Acta 72, 5997–6005.

Willbold, M., Elliott, T., 2017. Molybdenum isotope variations in magmatic rocks. Chem.

Geol. 449, 253–268.

Zhang, K., Zhu, X., Wood, R.A., Shi, Y., Gao, Z., Poulton, S.W., 2018. Oxygenation of the Mesoproterozoic ocean and the evolution of complex eukaryotes. Nat. Geosci. 11, 345–350.

Zhang, X., Sigman, D.M., Morel, F.M.M., Kraepiel, A.M.L., 2014. Nitrogen isotope fractionation by alternative nitrogenases and past ocean anoxia. Proc. Natl. Acad. Sci. U.S.A. 111, 4782–4787.

Zheng, W., Gilleaudeau, G.J., Kah, L.C., Anbar, A.D., 2018. Mercury isotope signatures record photic zone euxinia in the Mesoproterozoic ocean. Proc. Natl. Acad. Sci. U.S.A. https://doi.org/10.1073/pnas.1721733115.